Geophys. J. Int. (2005) **162,** 479–493 doi: 10.1111/j.1365-246X.2005.02666.x

Upper-mantle seismic structure in a region of incipient continental breakup: northern Ethiopian rift

Ian D. Bastow,[1] Graham W. Stuart,[1] J-Michael Kendall[1] and Cynthia J. Ebinger[2]

[1] *School of Earth and Environment, University of Leeds, Woodhouse Lane, Leeds,* LS2 9JT, *UK. E-mail: ibastow@earth.leeds.ac.uk*
[2] *Department of Geology, Royal Holloway University of London, Egham, Surrey, UK*

Accepted 2005 April 21. Received 2005 February 17; in original form 2004 October 7

SUMMARY

The northern Ethiopian rift forms the third arm of the Red Sea, Gulf of Aden triple junction, and marks the transition from continental rifting in the East African rift to incipient oceanic spreading in Afar. We determine the *P*- and *S*-wave velocity structure beneath the northern Ethiopian rift using independent tomographic inversion of *P*- and *S*-wave relative arrival-time residuals from teleseismic earthquakes recorded by the Ethiopia Afar Geoscientific Lithospheric Experiment (EAGLE) passive experiment using the regularised non-linear least-squares inversion method of VanDecar. Our 79 broad-band instruments covered an area 250 × 350 km centred on the Boset magmatic segment ∼70 km SE of Addis Ababa in the centre of the northern Ethiopian rift. The study area encompasses several rift segments showing increasing degrees of extension and magmatic intrusion moving from south to north into the Afar depression. Analysis of relative arrival-time residuals shows that the rift flanks are asymmetric with arrivals associated with the southeastern Somalian Plate faster (∼0.65 s for the *P* waves; ∼2 s for the *S* waves) than the northwestern Nubian Plate. Our tomographic inversions image a 75 km wide tabular low-velocity zone ($\delta V_P \approx -1.5$ per cent, $\delta V_S \approx -4$ per cent) beneath the less-evolved southern part of the rift in the uppermost 200–250 km of the mantle. At depths of >100 km, north of 8.5°N, this low-velocity anomaly broadens laterally and appears to be connected to deeper low-velocity structures under the Afar depression. An off-rift low-velocity structure extending perpendicular to the rift axis correlates with the eastern limit of the E–W trending reactivated Precambrian Ambo–Guder fault zone that is delineated by Quaternary eruptive centres. Along axis, the low-velocity upwelling beneath the rift is segmented, with low-velocity material in the uppermost 100 km often offset to the side of the rift with the highest rift flank topography. Our observations from this magmatic rift zone, which is transitional between continental and oceanic rifting, do not support detachment fault models of lithospheric extension but instead point to strain accommodation via magma assisted rifting.

Key words: rifts, seismic structure, tomography, upper-mantle.

1 INTRODUCTION

1.1 Background

Most passive margins worldwide are considered to be 'magmatic margins', characterized by thick sequences of extruded and underplated igneous rocks emplaced prior to, or during, rifting (e.g. Menzies *et al.* 2002). Despite their global abundance, however, the breakup history of magmatic passive margins is not well understood because the ocean–continent boundary is concealed by thick seaward dipping reflectors (e.g. Holbrook & Kelemen 1993). Reconstructions of conjugate margins globally show a marked asymmetry, with a lateral offset in the high strain zones within the crust and/or upper mantle (e.g. Louden & Chian 1999). This asymmetry has been cited as evidence that detachment faults accommodate large strains and mark the breakup boundary (e.g. Wernicke 1985; Lister *et al.* 1986). Alternatively, Ebinger & Casey (2001) and Buck (2004) propose that localized magma injection accommodates strain at breakup and border fault detachments are abandoned as melt volume increases during progressive extension.

The Ethiopian rift forms the third arm of the Red Sea, Gulf of Aden rift–rift–rift triple junction where the Arabian, Nubian, Somalian and Danakil plates join in Afar. The Miocene–Recent East African rift in Ethiopia subaerially exposes the transitional stage of rifting within the youngest continental flood basalt province worldwide, making it an ideal study locale for continental breakup processes. The Ethiopia Afar Geoscientific Lithospheric Experiment (EAGLE) probed the crust and upper-mantle structure in this region using passive and controlled source seismological techniques (Maguire *et al.* 2003) to examine the lithospheric structure of

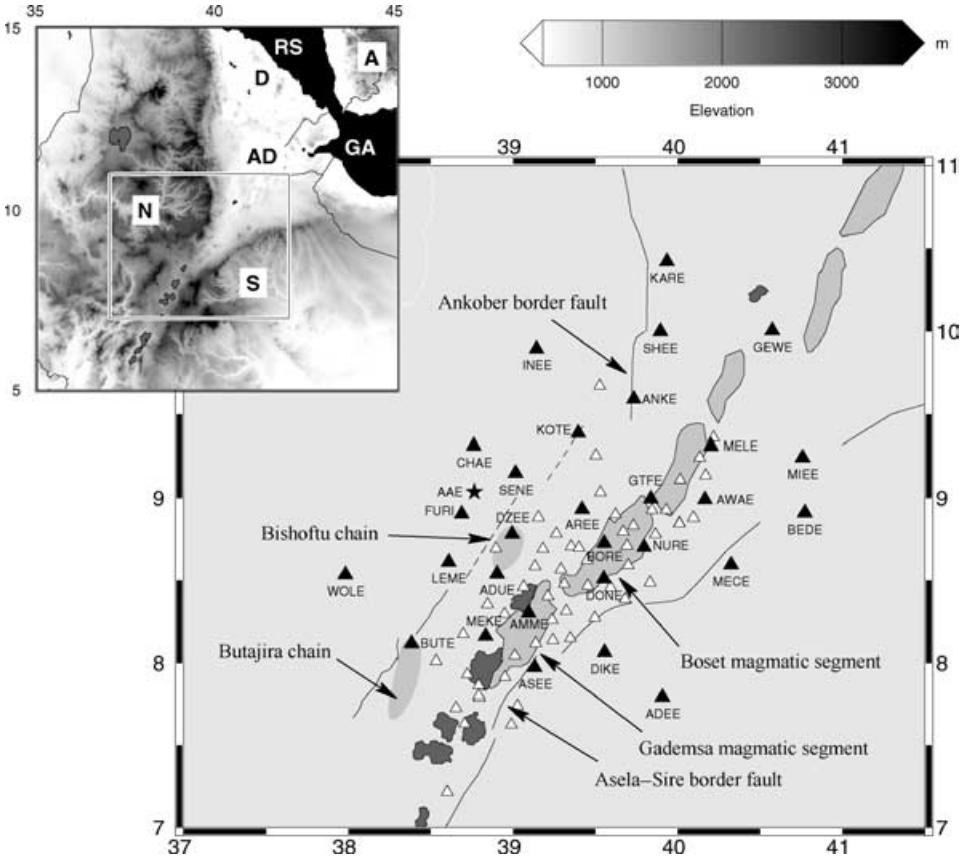

Figure 1. The location of the EAGLE passive network. Filled triangles are the EAGLE phase I passive experiment (2001 October—2003 January) and permanent station FURI. Open triangles are the EAGLE phase II passive experiment (2002 November—2003 February). Station AAE (Addis Ababa) is shown by the black star. Major Mid-Miocene border faults and Quaternary magmatic segments are also shown by the heavy black lines. Dashed lines are faulted monoclines. Inset: the regional tectonic setting on a topographic map. RS, Red Sea; GA, Gulf of Aden; A, Arabian Plate; AD, Afar Depression; D, Danakil microplate; N, Nubian Plate; S, Somalian Plate.

incipient oceanic spreading and continental margin formation. An aim central to EAGLE was to examine the correlation between higher strain magmatic segments and upper-mantle velocity structure, and resulting implications for melt extraction and along axis segmentation in a rift transitional between continental rifting and oceanic spreading.

The EAGLE phase I and II passive experiments consisted of 79 broad-band seismometers over an area 250 × 350 km centred on the Boset magmatic segment ∼70 km SE of Addis Ababa in the centre of the Ethiopian rift (Fig. 1). Here, we present the results of a study of the upper-mantle velocity in the region as revealed using body wave traveltime tomography. We adopt the method of VanDecar (1991) to image upper-mantle heterogeneities using regularised non-linear least-squares inversion of relative arrival-time residuals from teleseismic earthquakes. With a network aperture of ∼300 km, station spacing of 10 km within the rift valley and 40 km on the rift flanks, we are able to image with good resolution depths between 40 and 300 km (Evans & Achauer 1993).

1.2 Tectonic setting

The broad ∼2500 m high Ethiopian Plateau is capped by ∼2 km of flood basalts and rhyolites, which were erupted between 31 and 29 Ma (e.g. Hofmann *et al.* 1997; Ukstins *et al.* 2002), prior to, or concomitant with, the onset of rifting in the Red Sea and Gulf of Aden at ∼29 Ma (Wolfenden *et al.* 2004). The large volume of material and relatively short time interval of eruption are indicative of hot upper mantle beneath the plateau region, but the location and number of plumes or upper-mantle convective cells remain disputed (e.g. Ebinger & Sleep 1998; George *et al.* 1998; Courtillot *et al.* 1999). The motion of the large, slow moving Nubian Plate is relatively poorly constrained, but Ethiopia would have moved 300–600 km NW since 31 Ma relative to a fixed hotspot reference frame (e.g. Gripp & Gordon 2002).

The Ethiopian rift, the third arm of the triple junction, developed after the Red Sea and Aden rifts. Extension in southwestern Ethiopia and northern Kenya commenced by 20 Ma with central and northern rift sectors developing between 18 and 12 Ma, respectively (e.g. WoldeGabriel *et al.* 1991; Wolfenden *et al.* 2004). Large offset border faults commonly marked by chains of silicic centres formed along one or both sides of the rift. Since 12 Ma, strain progressively localized to the central rift valley where the loci of extension are en echelon chains of eruptive magmatic centres, dikes and small offset faults: magmatic segments (Ebinger & Casey 2001), Fig. 1.

Geodetic data indicate that the northern Ethiopian rift is currently extending in a direction 94°NE at 7 mm yr^{-1} (Fernandes *et al.* 2004), with 80 per cent of the strain localized at magmatic segments (Bilham *et al.* 1999). This evidence has been used to suggest that magmatic emplacement, not border faulting, increasingly dominates the rifting process after the initial stages of breakup (Ebinger & Casey 2001).

1.3 Previous seismological work

Using teleseismic receiver function analysis, Hebert & Langston (1984) estimated a Moho depth of 41 km beneath station AAE (Fig. 1); Dugda *et al.* (2005) show that crustal thickness varies from 25–31 km within the Ethiopian rift and Afar depression, and up to 42 and 44 km beneath the eastern and western plateaus, respectively. The most detailed information about crustal structure in Ethiopia, however, comes from seismic refraction studies. Makris & Ginzburg (1987) revised the results of Berckhemer *et al.* (1975) to indicate Moho depths of 33–44 km along an E–W refraction profile on the western plateau. Within the rift itself, the Moho depth varies from 30 km near EAGLE station AWAE (Fig. 1) to 26 km in Afar at ∼10°N. Most recently the EAGLE cross-rift and axial refraction profiles show that the crust thins from 30–35 km in the southern part of our study area to 25–28 km in the northern part (Maguire *et al.* 2003). The rift plateaus show asymmetry; the northern section of the western plateau is characterized by a 50 km thick crust with an ∼10 km high-velocity lower-crustal layer absent from the 40 km thick eastern plateau (Mackenzie *et al.* 2005). This high-velocity material is interpreted as underplate. The southern section of the western plateau is characterized by an ∼35 km crust (Dugda *et al.* 2005). Tomographic studies of the uppermost 15 km of crustal structure beneath the central rift zone show that the Quaternary magmatic segments are underlain by high-velocity ($V_P > 6.5$ km s^{-1}) elongate bodies (Keranen *et al.* 2004). These are interpreted as cooled mafic intrusions, which fed dykes and intrusions in the magmatic segments (Keranen *et al.* 2004).

Using Rayleigh wave dispersion from earthquakes with paths crossing Afar, Knox *et al.* (1998) determine uppermost upper-mantle *S*-wave velocities beneath the region to be 0.2–0.8 km s^{-1} (4.5–18 per cent) slower than Preliminary Reference Earth Model (PREM) and infer that partial melt is required to explain the observations. Other surface wave dispersion studies such as Debayle *et al.* (2001) and a *P* tomographic study by Benoit *et al.* (2003) suggest that a low-velocity zone exists to at least 410-km depth beneath Afar.

Knowledge of the deepest structure beneath East Africa comes from recent global tomographic models (e.g. Ritsema & Allen 2003). These global tomographic images show a low-velocity zone rising from the core–mantle boundary beneath southern Africa and impinging on the Afro-Arabian lithosphere in the Afar triple junction zone. Montelli *et al.* (2004) claim that there is a link between upper- and lower-mantle low-velocity structure in the region by imaging a plume to depths in excess of 670 km beneath the Afar triple junction zone. However, receiver function analyses of the 410 and 660 km discontinuities do not indicate the expected thinning of the transition zone beneath the flanks of the Arabian shield (Benoit *et al.* 2003) and Afar (Nyblade *et al.* 2000). Therefore, a connection between this large-scale plume and upper-mantle seismic structures in Afar remains uncertain.

S-wave splitting observations within the East African rift are approximately rift parallel (e.g. Gashawbeza *et al.* 2004) and show a northward increase in delay times from Kenya (1.0 s) in the south to Djibouti (1.6 s) to the north (Ayele *et al.* 2004). They interpret these observations as a northward increase in either the alignment of melt in the upper 90 km of the lithosphere or lattice preferred orientation of olivine in the asthenosphere parallel to the rift axis as material flows laterally to fill the gap caused by lithospheric extension. Kendall *et al.* (2005) show that the maximum splitting directions mirror the orientation of Quaternary magmatic segments within the rift, interpreting these observations as due to rift parallel, melt-filled cracks penetrating the lithosphere and accommodating extension.

2 DATA

We determine relative arrival-time residuals from recordings of teleseismic earthquakes on 29 broad-band stations (EAGLE phase I), which were operational between 2001 late October and 2003 January (Fig. 1). Güralp CMG-3T and CMG-40TD instruments, with a natural period of 30 s, recorded data at 50 samples per second. Additional data came from 50 CMG-6TD instruments recording at 100 s.p.s. between 2002 November and 2003 February (EAGLE phase II) and the permanent IRIS GNS/GDSN station FURI. For security reasons, the stations were located in compounds attached to schools and clinics. The level of high-frequency cultural noise (>1 Hz) could be high during the daytime, reaching levels described by the high noise model of Peterson (1993). At night, however, noise levels were significantly reduced.

For the 16-month period of operation of the EAGLE passive experiment, waveforms from 442 events of magnitude mb $\geq$ 5.5 in the teleseismic epicentral distance (Δ) range $30^\circ < \Delta < 103^\circ$ were visually inspected for those with a good signal-to-noise ratio on at least 10 stations. For *P* waves, we finally analysed the recordings from 108 teleseismic earthquakes together with 11 earthquakes, which were at distances from which core (*PKP*) phases were recorded. Further visual inspection of 1000 lower magnitude earthquakes (4.4 < mb < 5.5) yielded a further 25 earthquakes to improve the uniformity of data coverage with respect to backazimuth and epicentral distance. *S*-wave arrivals were inspected in a similar fashion to yield a data selection of 39 *S*-wave and 18 *SKS* core phase earthquakes. Fig. 2 shows the distribution of these earthquakes with respect to the centre of the EAGLE passive network.

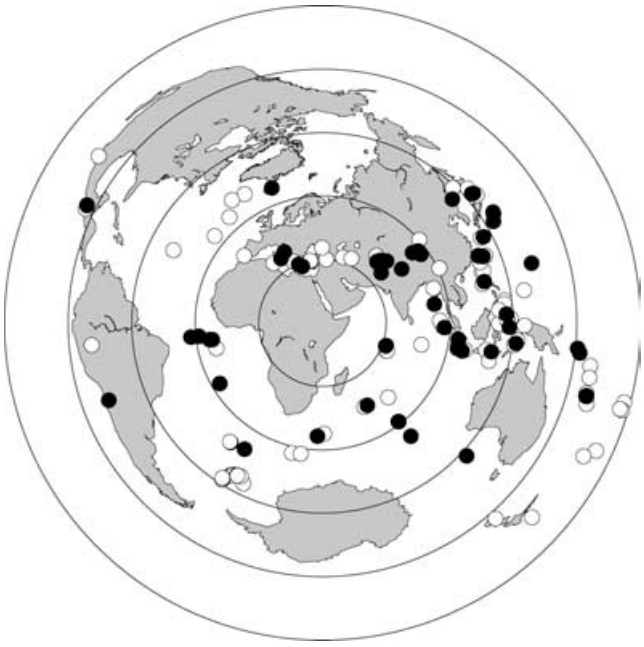

Figure 2. Backazimuth and distance distribution of earthquakes used in this study. The white circles represent epicentres with *P*-wave traveltime observations. Black circles represent earthquakes with both *P*- and *S*-wave traveltime observations. The concentric circles on the plot indicate 30° intervals from the centre of the EAGLE passive network at 9°N, 39°E.

3 METHOD

3.1 Method of relative arrival-time determination

Manual picking of the first arriving *P* or *S* waves identifiable across the network was performed on waveforms, which were filtered with a zero-phase two-pole Butterworth filter with corner frequencies of 0.4–2 Hz. Direct *S* waves were picked on transverse component seismograms to minimize contamination by *P* and *P*-to-*S* converted phases and were filtered between 0.04–0.1 Hz. *SKS* core phases were picked on radial component seismograms. Phase arrivals were later more accurately determined using the multichannel cross-correlation (MCCC) technique of VanDecar & Crosson (1990) using the same bandpass filters. Filter bandwidths were designed to retain the higher frequencies because our inversion procedure adopts ray theory (the infinite frequency approximation). We found, in agreement with VanDecar & Crosson (1990), that the exact choice of filter has a negligible effect on the final relative arrival times determined. Our chosen bandwidths are similar to those used in other teleseismic tomographic studies in both oceanic island settings (e.g. Allen *et al.* 2002: *P*, 0.8–2 Hz; *S*, 0.03–0.1 Hz) and quieter shield areas (e.g. Sol *et al.* 2002: *P*, 0.4–2 Hz; *S*, 0.04–1.6 Hz).

During the MCCC procedure of VanDecar & Crosson (1990), we selected a window (3 s for *P* and 12 s for *S* waves) to cross-correlate, containing the initial phase arrival and typically one or two cycles of *P*- or *S*-wave energy. This minimized contamination by secondary arrivals. All pairs of windowed traces for a given event were cross-correlated and relative arrival times Δt_{ij} between pairs of stations i, j were obtained (VanDecar & Crosson 1990). Our relative arrival times for each station were then retrieved by a least-squares minimization of the residual res_{ij} for all station pairs where

$$res_{ij} = \Delta t_{ij} - (t_i - t_j), \tag{1}$$

where t_i and t_j are the arrival times associated with the ith and jth traces, respectively.

The MCCC method provides a means of quantifying the error associated with each arrival time. The standard deviation σ_i of the distribution of the residuals (res_{ij}) associated with the ith trace is determined by

$$\sigma_i = \sqrt{\frac{1}{(n-2)} \sum_{j \neq i} res_{ij}^2}, \tag{2}$$

where i, j represent the pairs of the n stations. In this study, relative arrival times determined in this way have mean standard deviations 0.02 and 0.05 s for *P* and *S* waves, respectively. Comparable arrival-time error estimates found in other studies in quiet cratonic regions (e.g. the Canadian shield; Sol *et al.* 2002) are 0.02 s for *P* waves and 0.05 s for *S* waves, and in oceanic island regions where stations suffer higher levels of microseismic noise (e.g. Iceland; Allen *et al.* 2002) are 0.1 s for *P* waves and 0.25 s for *S* waves. Tilmann *et al.* (2001) compared traveltimes of earthquakes with hypocentres very close to one another to find the errors to be $\sim \pm 0.05$ s, higher than their MCCC derived estimates, which were often less than the sample rate of 0.01 s. We also consider that the MCCC derived estimates of timing uncertainty presented here are most likely too small.

Relative arrival-time residuals t_{RES} for each station are given by

$$t_{\mathrm{RES_i}} = t_i - (t_{\mathrm{e}_i} - \overline{t_{\mathrm{e}}}), \tag{3}$$

where t_i is the relative arrival time for each station i, t_{e_i} is the expected traveltime based on the IASP91 traveltime tables (Kennett & Engdahl 1991) for the ith station and $\overline{t_{\mathrm{e}}}$ is the mean of the IASP91 predicted traveltimes associated with that particular event.

Our final traveltime data sets comprise 3243 *P* traveltimes and 1150 *S* traveltimes whose distributions with backazimuth and epicentral distance are illustrated in Fig. 2.

3.2 Analysis of relative arrival-time residuals

International Seismological Catalogue (ISC) traveltime data for the period 1994 December—1997 September were analysed for the permanent station AAE in Addis Ababa (Fig. 1). These data, consisting of 4277 *P* arrivals, indicate that the mean absolute delay time with respect to the IASP91 traveltime tables for *P* waves arriving at AAE is 4.6±0.15 s (2× standard error); this makes AAE one of the slowest stations on Earth (e.g. Poupinet 1979). Even accounting for the effects of topography (∼3 km producing a delay of ∼0.5 s relative to the IASP91 traveltime tables), this mean delay time translates into a 4.1 s, ∼5 per cent slow-velocity anomaly in the upper mantle (0–410 km) beneath the station. It must therefore be kept in mind that our relative arrival-time residuals are on an absolute traveltime 'pedestal' of ∼4 s relative to the global average.

Fig. 3(a) shows the variation in mean station relative arrival-time residuals across the rift. These data have been corrected to a datum of 600 m (lowest station) using a correction velocity for the uppermost crust of 3.5 km s^{-1}. The error bars do not represent data quality but show one standard deviation from the mean of the relative arrival-time residuals for each station and reflect variations of traveltimes with backazimuth. Fig. 3(b) shows the mean relative arrival-time residuals for EAGLE phase I stations in map form. The mean residuals on the rift flanks are different, with arrivals associated with the eastern Somalian Plate faster (∼0.65 s for the *P* waves; ∼2 s for the *S* wave data) than those for the western Ethiopian Plateau on the Nubian Plate.

Fig. 4 shows plots of *P*-wave relative arrival-time residuals as a function of backazimuth and epicentral distance for stations CHAE, DIKE and AREE (Fig. 1). Station DIKE, on the eastern rift flank, has relatively fast arrivals (−0.32 s) associated with arrivals coming from easterly directions. Earthquakes with rays through the rift from more westerly and northerly directions have traveltimes that are relatively slower by ∼1 s. In contrast, station CHAE, located on the western rift flank shows the fastest and slowest arrivals are those from northerly and easterly azimuths respectively, with a peak-to-peak variation of ∼1.25 s. We infer from these observations that the mantle beneath the rift is underlain by low-velocity structure. Station AREE, located within the rift valley, shows little azimuthal variation in relative arrival-time residuals that are, on average, positive (0.37 s) indicating that it is more central to a regional low-velocity structure.

3.3 Model parametrization and inversion procedure

The scheme used in this study to invert relative arrival-time residuals for velocity perturbations beneath the northern Ethoipian rift is that of VanDecar (1991). Several studies have successfully used this method, e.g. in the Cascadia subduction zone (VanDecar 1991) and in Brazil (Schimmel *et al.* 2003).

We parametrize *P*- and *S*-wave slowness using B-splines under tension over a dense grid of knots (Cline 1981). Interpolation between slowness values at each knot allows the generation of smooth velocity models through which ray tracing can be performed. The equilateral grid consists of 25 knots in depth between 0–600 km, 45 knots in latitude between 4–14°N and 49 knots in longitude between 34.5–44.5°E for a total of 55 125 knots parametrizing slowness. The knot spacing is 15 km in the innermost resolvable parts

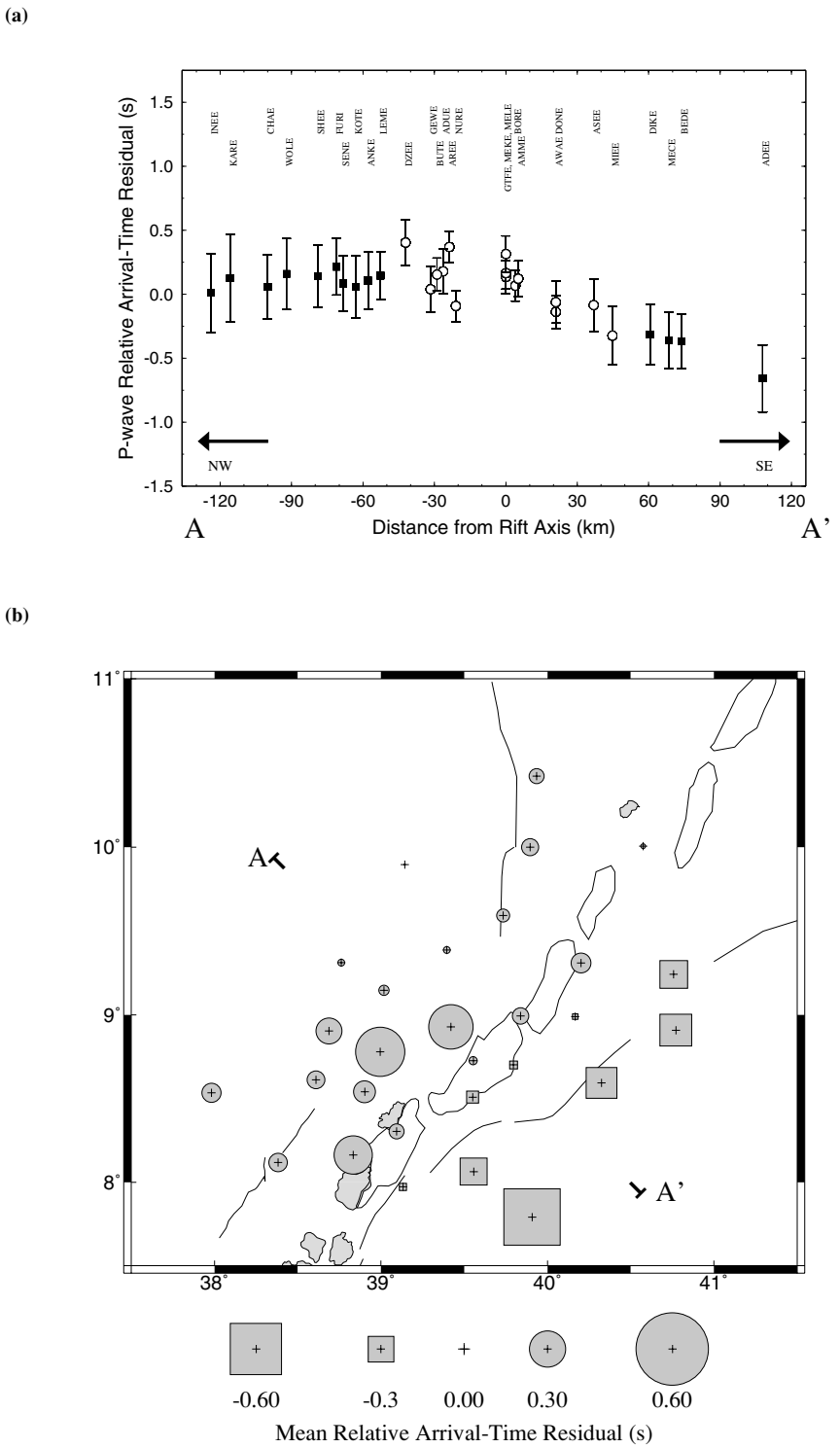

Figure 3. (a) Cross-rift profile of mean relative arrival-time residuals for *P* waves. Each station is projected onto a cross-rift line A–A′ running NW–SE across the EAGLE phase I network. The open circles indicate a station located within the rift valley and the black squares indicate a station located outside the rift valley. The error bars represent one standard deviation from the mean of the relative arrival-time residuals for each station. (b) Map plot of mean *P*-wave relative arrival-time residual data. Squares represent stations with negative relative arrival-time residuals (relatively fast). Circles represent stations with positive relative arrival-time residuals (relatively slow).

(7–11°N, 37–42°E, 0–150 km depth). Outside this region, knot spacing increases to 30 km between 150 and 400 km, and then to 50 km between 400 and 600 km. Thus we will be able to resolve structures with approximately 30 km spatial wavelength in the top 150 km. If we take the size of the Fresnel zone at depth to be of the order $(\lambda L)^{1/2}$, for a wave of wavelength λ and ray length L (e.g. Montelli *et al.* 2004), with L representing depth and λ determined by the highest frequency content of our data (2 Hz for *P* waves and 0.1 Hz

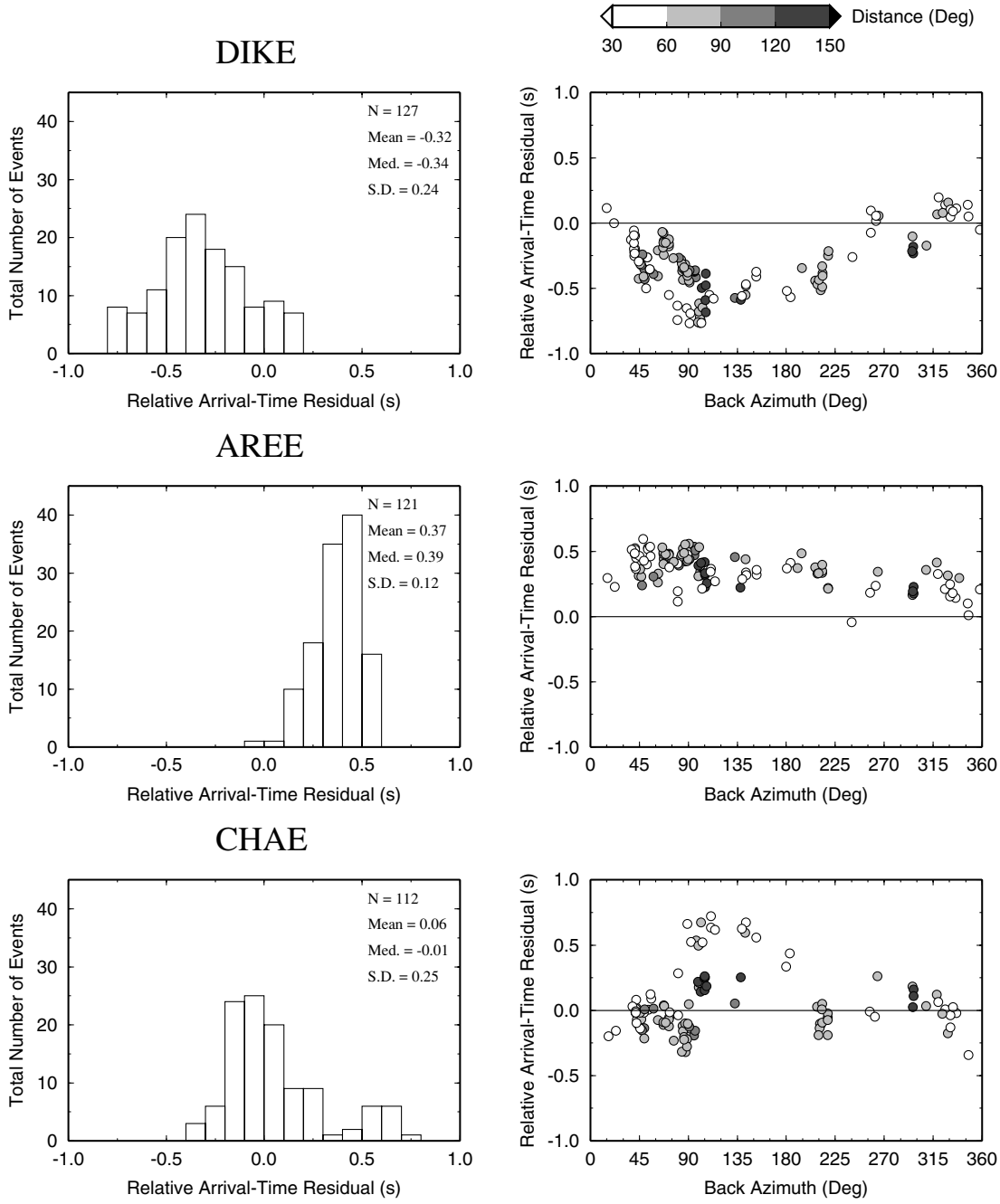

Figure 4. Variation of relative arrival-time residuals as a function of backazimuth and epicentral distance from stations DIKE, AREE and CHAE (Fig. 1). Negative arrival times indicate a relatively fast arrival, whilst positive arrival times indicate a relatively slow arrival. Med. = median, S.D. = standard deviation.

for *S* waves), we could justify resolution of structures approaching a lower limit of ∼14 and ∼47 km in the uppermost parts of our model for the *P*- and *S*-wave inversions, respectively. We keep the same parametrization scheme for the lower resolution *S*-wave inversion because we suppress spatial gradients in order to regularise the inversion and so never interpret features of wavelength less than the Fresnel zones. Tests have shown that the images we recover are independent of knot position.

We parametrize outside the area of interest so that we do not map unwarranted and spurious structure into the region where we will be making our structural interpretations, i.e. a minimum structure approach (VanDecar 1991). However, we do not parametrize deeper than 600 km because we have found through the analyses of synthetic tests that this is the shallowest depth that allows us to successfully differentiate between heterogeneities in the resolvable (i.e. where we have crossing rays) uppermost 300 km of the model from deeper unresolvable parts of the model. A deeper parametrization scheme results in the unnecessary loss of velocity structure from the top 300 km.

In the regularised non-linear least-squares inversion procedure, we solve simultaneously for velocity perturbations, station terms and source terms (VanDecar 1991). The station static terms are free parameters used in the inversion procedure to absorb traveltime anomalies associated with the region directly beneath the station

where the lack of crossing rays prevents the resolution of crustal structure. A free-parameter source term is included in the inversion to account for small variations in backazimuth and incidence angle caused by distant heterogeneities and source mislocations.

Because our inverse problem is underdetermined (more unknowns than observations), even in the absence of errors we cannot expect to find a unique solution. We therefore choose to select a model that contains the least amount of structure (e.g. Constable *et al.* 1987; VanDecar 1991; Tilmann *et al.* 2001; Allen *et al.* 2002). We regularise through the minimization of a seven-point finite element approximation to the Laplacian operator in order to penalize the roughness (second derivative) of the final slowness model to produce a smooth model that fits the data. In addition, the outside knots (with the exception of the top layer) are heavily damped to zero anomaly so that the 3-D model can merge smoothly into the surrounding radial Earth. The non-linearity of the problem is addressed in the inversion procedure by performing 3-D ray tracing through successive linear inversion models. We have found in this study that no significant change in image occurs after two iterations of linear inversion and 3-D ray tracing, with an ∼6 per cent loss of rays. By investigating the trade-off between the rms residual reduction (the per cent difference between the initial weighted and final rms misfit to the traveltime equations) and rms model roughness, we select a preferred model that fits the data well but does not account for more relative arrival-time residual reduction than can be justified by our *a priori* estimation of data noise levels. All models in this study account for 92 per cent (from 0.38 to 0.03 s) of the rms relative arrival-time residuals for *P* waves and 89 per cent (from 1.32 to 0.14 s) for *S* waves. We are, therefore, treating our MCCC derived estimates of rms timing uncertainty as optimistic bounds when fitting the data. Subtracting the station terms from the delay times reduces the rms relative arrival-time residuals from 0.38 to 0.24 s for *P* waves and from 1.32 to 1.00 s for *S* waves; these corrected residuals more accurately reflect the proportion of the delay-time anomalies that will be mapped into the region of the model where we make our interpretations.

4 RESOLUTION

We seek to assess the linear resolving power of the inversion technique by analysing the ability of our ray geometry to retrieve a standard checkerboard model using ray paths through a 1-D earth. This is often as far as some authors go using VanDecar's code (e.g. Sol *et al.* 2002). A realistic synthetic rift structure is used to test non-linear resolution when the traveltimes are determined by ray tracing through the 3-D structure.

In the checkerboard test, we place positive and negative slowness-anomaly (±5 per cent, 25 km diameter) spheres (described by Gaussian functions across their diameter) throughout the upper 300 km of model space (Fig. 5) in order to assess the retrievability of structures of wavelength similar to the magmatic segments we observe at the surface (Fig. 1). Two 50 km diameter spheres at depths of 500 km are located at $8.5^\circ N$, $39^\circ E$ and $11^\circ N$, $42^\circ E$ and simulate low-velocity heterogeneity, which may exist outside our volume of interest (e.g. under Afar). The checkerboard approach allows us to assess the sensitivity of our model by highlighting areas of good ray coverage and the extent to which smearing of anomalies is occurring in a simple linear inversion.

We invert for these synthetic velocity structures using identical model parametrization and inversion regularization as used in the inversion of the observed data and using ray paths through a 1-D Earth as defined by the IASP91 traveltime tables. A Gaussian residual time error component with a standard deviation of 0.02 and 0.05 s for the *P*- and *S*-wave data respectively is added to the theoretical traveltimes (the standard deviation of noise estimated for our real data). Fig. 5 shows the recovered velocity structure from the checkerboard test. The spheres retrieved are distinct from one another (separated by zero anomaly structure), indicating good lateral resolution to depths of 300 km. Lateral resolution and the recovery of the amplitudes of the velocity anomalies (∼30 per cent) are best at 150 km where we expect a seismic network of our dimensions to have the highest density of crossing rays (e.g. Ritsema *et al.* 1998). Although vertical smearing of the anomalies does exist, it is clear that the low-velocity structure in the lower (500 km) parts of the model is not smeared into the upper 300 km of the model space.

The diagnostic value of this checkerboard approach to resolution assessment is limited because it does not test the non-linearity or the accuracy of the linearization approximations (van der Hilst *et al.* 1993). We choose to assess non-linear resolution by computing traveltimes through a synthetic rift model that simulates the kind of structure we see from our real data inversions. This model (Fig. 6) has rift flanks (peak velocity perturbation $\delta V_P = +3$ per cent) and a tabular low-velocity body (peak velocity perturbation $\delta V_P = +5$ per cent) beneath the centre of the rift. The high- and low-velocity anomaly bodies are defined by Gaussian functions across their width and extend with peak anomaly to 200 km depth, falling to zero anomaly at ∼250 km depth. Synthetic traveltimes are computed after ray tracing through the synthetic velocity model. The inversion results are obtained after starting with rays projected through a spherically symmetric earth; and iterating towards a final solution through a series of two linear inversions and 3-D ray tracing (Fig. 6). The synthetic rift model can be successfully retrieved to depths approaching 250 km. The amplitude of recovered anomalies is ∼50 per cent of the input values. There is very little lateral offset of the low-velocity tabular body from its central location along strike from the continental to oceanic settings of the study area. There is no apparent along axis segmentation due to preferential recovery of amplitudes along the tabular low-velocity body. There is some vertical smearing in our retrieved model with the peak anomaly region of the central rift stretched by ∼50 km to almost 250 km depth.

Fig. 6 also shows the results of our *S*-wave synthetic rift model, which has initial peak velocity anomaly amplitudes of $\delta V_S = -10$ per cent and $\delta V_S = 6$ per cent for the rift and rift flanks, respectively. The results show that the rift model can be successfully retrieved using the smaller *S*-wave data set but the extent of vertical smearing is greater than in the *P*-wave case.

Anomalies in the top 40 km where there are few crossing rays are poorly resolved and are taken account of by station static terms in the inversion procedure. For a synthetic rift model where the peak low-velocity anomaly extends from just below 0 to 200 km depth, the station statics sensibly account for the unresolvable crustal structure (Fig. 6b). As expected, for the case where the peak anomaly extends from 75 to 200 km, the station static terms fall to almost zero. Therefore, structures we present herein at depths ≥75 km are independent of crustal structure.

5 UPPER-MANTLE SEISMIC STRUCTURE

In Fig. 7, depth slices through the *P* velocity model show a low-velocity anomaly of $\delta V_P = -1$ to -1.5 per cent, which is largely confined to the region beneath the rift valley. The lithosphere beneath

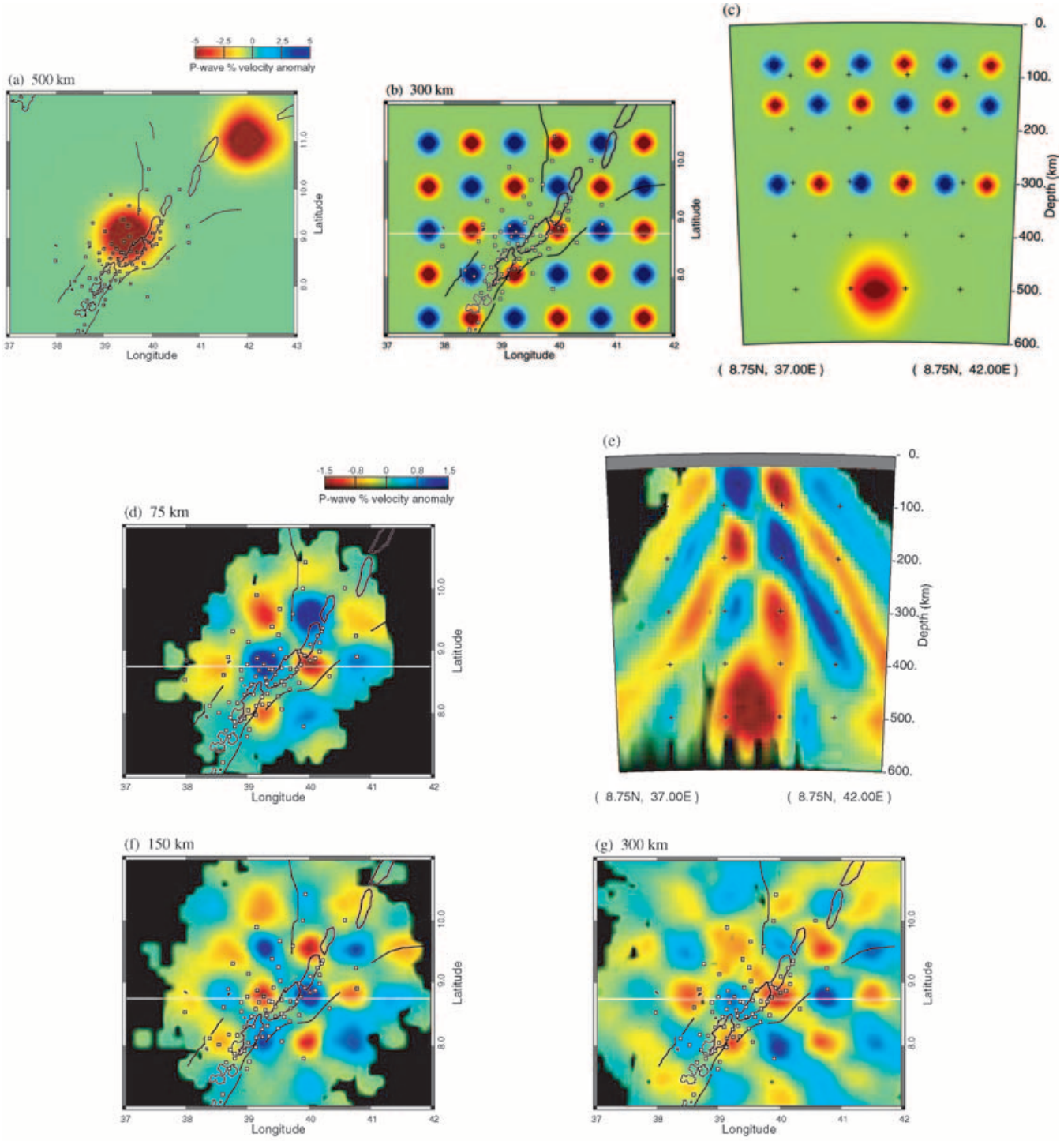

Figure 5. (a and b) Depth slices through the synthetic checkerboard model at 500 and 300 km depth, respectively. (c) A cross-section (shown on b as a white line) through the input model. 25 km diameter spheres (defined by Gaussian functions across their diameter) of $\delta V_P = \pm 5$ per cent peak anomaly are distributed in layers of depth 75, 150 and 300 km in order to simulate small-scale velocity heterogeneity in the uppermost mantle beneath the study area. The 500 km deep, 50 km-diameter $\delta V_P = -5$ per cent peak anomaly sphere at 11°N, 42°E is specifically designed to simulate heterogeneity beneath the Afar region. (d, f and g) Depth slices through the retrieved checkerboard model at 75, 150 and 300 km depth. (e) A cross-section through the retrieved checkerboard model. The grey band at the top of cross-section (e) precludes the view of the uppermost unresolved part of the model where ray paths are almost all parallel and vertical. Black lines show locations of Quaternary magmatic centres and Mid-Miocene border faults. Areas of low ray density (less than 10 rays per 15 km^3) are black.

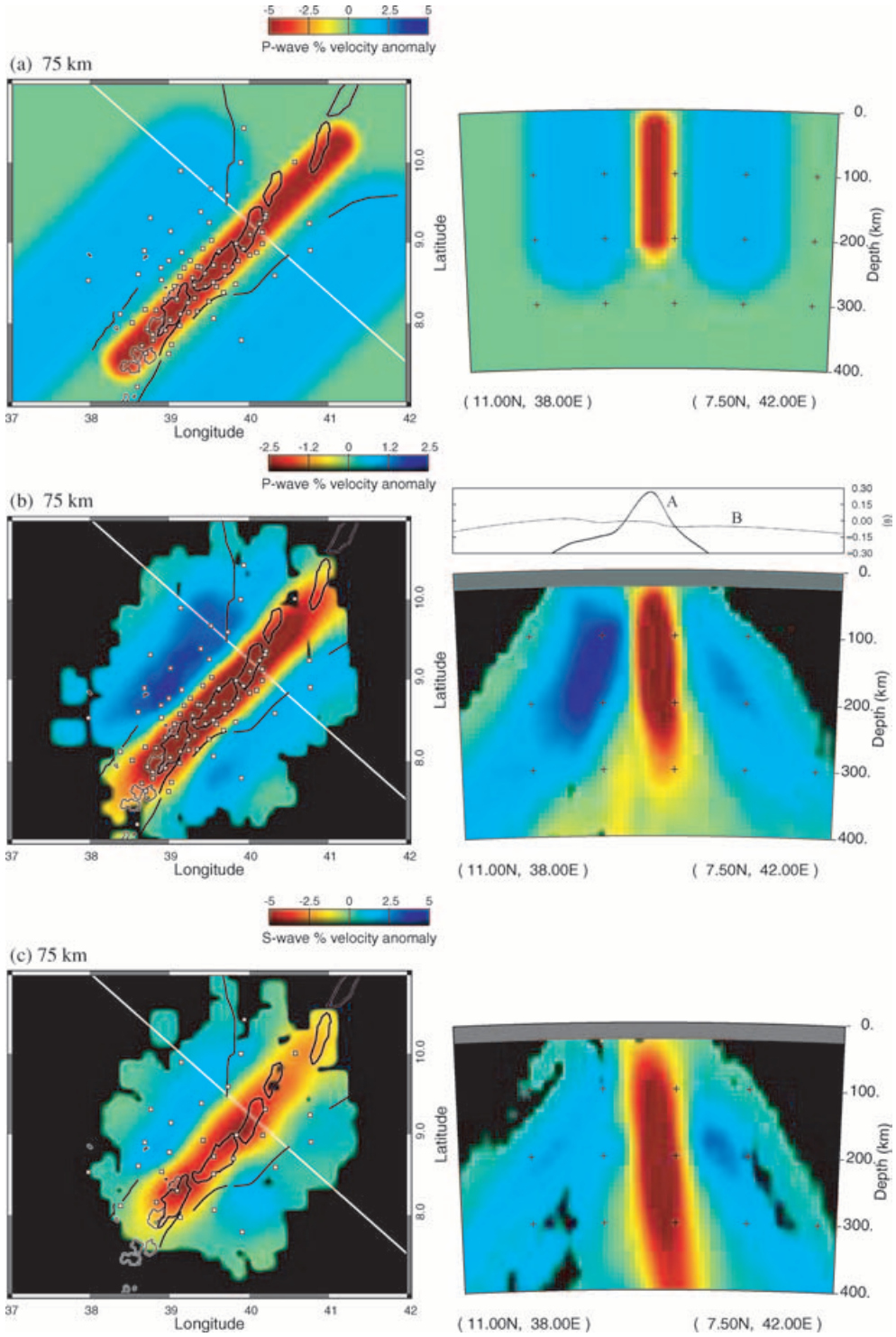

Figure 6. (a) Depth slice (left) through input *P*-wave synthetic rift model at 75 km depth. The white line on this figure indicates the location of the cross-section (right). (b) Depth slice (left) and cross-section (right) through the recovered *P*-wave synthetic rift model. (c) Depth slice (left) and cross-section (right) through the recovered *S*-wave synthetic rift model. The lines marked A on the profile plotted above cross-section (b) shows the cross-rift variation in station statics for the synthetic rift structure inversion. The line marked B in (b) shows that the statics drop to almost zero for the case when synthetic velocity structure is placed between 75–200 km depth.

rift flanks is characterized by faster (up to $\delta V_P = +1$ per cent) velocity structure. Along the length of the Ethiopian rift, the low-velocity anomaly is not located directly beneath the magmatic segments in the centre of the rift. In some cases (such as around 8°N, 39°E near the Ankober border fault, and 9.5°N, 40°E near the Asela–Sire border fault), it lies closer to the side of the rift with the higher rift flank topography (Figs 1, 7a, 8a and b). The morphology of the low-velocity structures is maintained to depths approaching 100 km but below this depth the low-velocity anomalies become more central about the rift axis. In the southern part of the Afar depression

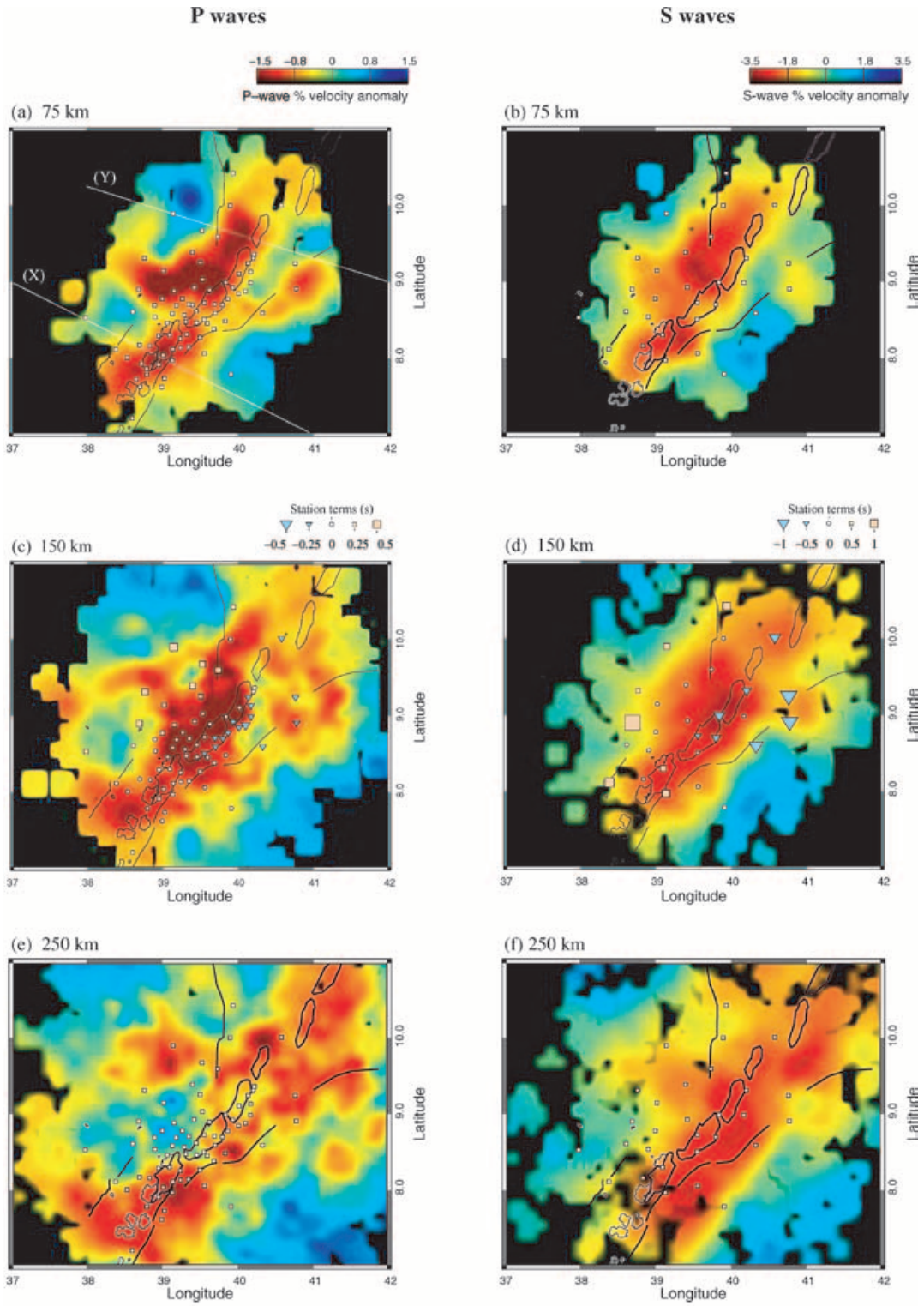

Figure 7. (a, c and e) Depth slices through the *P*-wave velocity model at 75, 150 and 250 km depth. (b, d and f) Depth slices through the *S*-wave velocity model at 75, 150 and 250 km depth. The locations of stations contributing to the tomographic inversions are shown with white squares in (a), (b), (e) and (f). Square and triangular symbols in (c) and (d) show the magnitude and sign of station static terms.

north of 10°N, the low-velocity zone shifts eastwards and follows the trend of the younger Ethiopian rift, which is thought to overprint the late Oligocene Red Sea and Gulf of Aden rift structures (Wolfenden *et al.* 2004).

A limb of low-velocity structure extends from the NNE-trending Ethiopian rift to the west of 9°N, 39°E and extends more than 100 km in a westerly direction from the Quaternary magmatic segments in the centre of the rift. This limb corresponds to an area of lower relief

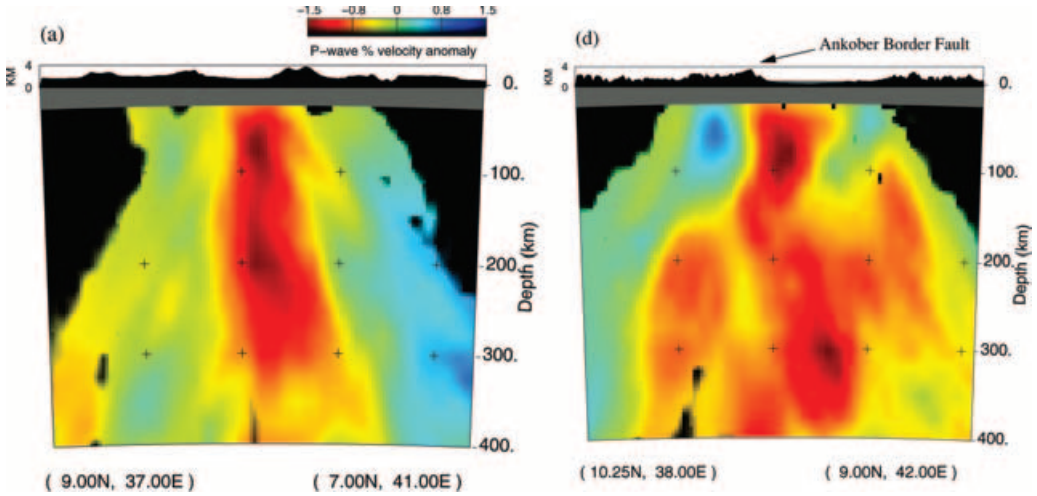

Figure 8. (a) A vertical cross-section through the *P*-wave velocity model in the continental rifting part of the model. (b) A cross-section through the transitional rifting region towards Afar. The orientations of cross-sections (a) and (b) are shown as white lines X and Y on Fig. 7(a)

bounded to the north by the E–W striking Precambrian Guder–Ambo fault zone (Mohr 1967) and the rift parallel Bishoftu chain (e.g. WoldeGabriel 1988), and is characterized by numerous Quaternary eruptive centres (e.g. Abebe *et al.* 1998; Chernet *et al.* 1998). Another isolated anomaly underlies the southern margin of the Aden rift, near station MIEE (Figs 1 and 7a). A large Late Miocene trachytic eruptive centre, Gara Gumbi, lies above the eastern side of this velocity anomaly (e.g. Chernet *et al.* 1998).

Cross-sections through the *P* velocity model (Fig. 8) show that in the southern, less extended parts of the rift, the low-velocity anomaly is narrow (∼75 km wide) and tabular in shape. In contrast, further north, the low-velocity anomaly broadens laterally below 100 km. Along strike, the depth extent of low-velocity structure increases from ∼250 km (allowing for ∼50 km vertical smearing based on our synthetic rift model results) south of 9°N to more than 300 km towards Afar. The region of the N–S Ankober border fault on the western side of the rift valley (around 9.5°N, 39.5°E) shown in cross-section in Fig. 8(b) shows a sharp contrast between high- and low-velocity structure at the flanks of the rift with peak-to-peak amplitude of $\delta V_P = 2.5$ per cent. The reduction of velocity anomaly amplitude with depth at ∼100 km is similar to estimates of lithospheric thicknesses of ∼90 km for the Ethiopian plateau beneath FURI (Ayele *et al.* 2004).

These first-order observations of velocity heterogeneities observed in slices through the *P* velocity model are confirmed by images of the independently inverted *S*-wave data. Fig. 7(b) shows that the upper mantle at 75 km beneath the rift is characterized by a low-velocity anomaly of up to $\delta V_S = -4$ per cent whilst the flanks are faster (up to $\delta V_S = 1.5$ per cent). The offsets and segmentation of the low-velocity structure are evident but less clear than for the *P* inversion due to the smaller number of rays in the model, the larger seismic wavelengths and higher noise levels associated with the *S*-wave data. Station static terms computed during the inversion are shown in Figs 7(c) and (d).

6 DISCUSSION

6.1 Contrasts in rift flank structure

The striking first-order observation of the cross-rift profile of relative arrival-time residuals (Fig. 3) is its asymmetric nature with faster arrivals associated with the eastern Somalian Plate compared with the Nubian Plate. Seismic data confirm that a proportion of plateau uplift and rift flank asymmetry can be explained by crustal thickness variations. Crust of thickness ∼50 km underlies the Nubian Plate margin and Mackenzie *et al.* (2005) infer that this crustal thickness difference may be due to plume related underplate (∼10 km).

Gravity–isostacy relations indicate that there may be a remaining component of dynamic uplift beneath the western Ethiopian plateau (e.g. Ebinger *et al.* 1989; Tiberi *et al.* 2004). Tiberi *et al.* (2004) suggest that ∼2 km of uplift is isostatically compensated by crustal thickness variations (underplating), with a further ∼500 m of uplift attributed to dynamic processes. Our observed relative arrival-time residual data cannot be entirely explained by crustal thickness variations alone so there must be a lithospheric and/or asthenospheric component to our observations. The NW part of Fig. 7(a), for example, corresponds with the highest plateau elevation in our study area. Fig. 8(b) shows that this area is underlain by low-velocity material at depths ≥150 km, which may provide a component of dynamic buoyancy if we equate low velocity with low density.

Existing structural inheritances can play an important role in rift propagation (e.g. Vauchez *et al.* 1997). Abdelsalam & Stern (1996) show that the pre-Cambrian terrain boundaries and suture zones strike in a N–NNE direction in Ethiopia, subparallel to the rift. We cannot, therefore, rule out a model where the rift has developed at the juxtaposition of two different lithospheric units to explain our observed asymmetry in relative arrival-time residuals.

6.2 Comparisons with other rifts

The observed peak-to-peak variations (up to ∼1.25 s for *P* waves and 2.5 s for *S* waves) in relative arrival-time residuals between rift stations and rift flank stations are comparable with other active rifting areas such as Kenya (∼1 s for the rift flank stations, Achauer & Masson 2002). In Kenya, a low-velocity steep sided tabular body is imaged beneath the rift, similar to that which we image in the continental rifting southern part of our study area (Fig. 7d). These observations can be contrasted with the Rhine graben, which is interpreted as a passive rift because it is not characterized by significant upper-mantle low velocities (Achauer & Masson 2002). The Baikal rift (e.g. Gao *et al.* 2003; Tiberi *et al.* 2003) and the Rio Grande rift (e.g. Gao *et al.* 2004) are interpreted as rifts where small-scale convection patterns characterize the upper mantle beneath the rifts with no apparent connection to deeper (>300 km)

low-velocity structures. Davis & Slack (2002) have also interpreted Kenyan teleseismic traveltime data in terms of small-scale convection patterns that generate large velocity heterogeneities beneath the region.

In contrast to regions that are interpreted in terms of small-scale convection, our results are less easily interpreted in this way. Figs 8(a) and (b) show that the low velocities in the uppermost 100 km beneath the rift are narrow (<100 km wide) and tabular in shape, in contrast to the broader (>200 km wide) upper-mantle convection patterns observed at Baikal and Rio Grande. Fig. 8 gives some indication that low velocities beneath the northern (transitional and towards Afar) rifting parts of our study area extend to greater depths than in the southern (continental rifting) part.

The broadening of the low-velocity structures at depths >100 km, towards Afar corresponds with the direction of increasing extension of the northward propagating Ethiopian rift (e.g. Wolfenden *et al.* 2004), towards the older and more established sea floor spreading centres of the Red Sea and Gulf of Aden.

6.3 Partial melt or thermal anomaly?

Determining the cause of seismic heterogeneity within the Earth is not straightforward because a number of factors can affect seismic velocities. In the upper mantle, temperature is believed to have more influence than compositional variations (e.g. Goes *et al.* 2000), which are thought to be <1 per cent if there are no strongly depleted Mg-rich harzburgites present (Sobolev *et al.* 1996). Other factors affecting seismic velocities are the presence of partial melt or water (e.g. Sobolev *et al.* 1996). Anisotropy can also play a role in wave speed variations (e.g. Gao *et al.* 2004) but our good event coverage with respect to backazimuth means that our velocity models represent the average velocity structure in the region.

Goes *et al.* (2000) predicts that a 100°C increase in temperature is associated with a decrease in δV_P of 0.5–2 per cent and in δV_S of 0.7–4.5 per cent. Thus, the observed maximum peak-to-peak amplitudes of $\delta V_P \approx 2.5$ per cent and $\delta V_S \approx 5.5$ per cent (at ∼150 km) could, if attributed solely to temperature effects, translate to lateral temperature variations of 125–500°C and 122–800°C for the *P* and *S* wave inversions, respectively. The presence of melt, however, will reduce the temperature contrasts required to explain the anomalies. Kendall *et al.* (2005) predict partial melt in vertically oriented 'dikes' of magma rising from the base of the lithosphere based on their analyses of SKS shear wave splitting observations across the EAGLE network. Major element compositions of Quaternary magmatic products erupted in the Bishoftu and Butajira areas (Fig. 1) suggest the onset of melting occurs in the depth range 53–88 km (Rooney *et al.* 2005). When interpreted in light of these independent geochemical and geophysical data, the low-velocity zones observed beneath the Ethiopian rift and Afar depression, therefore, indicate anomalously hot upper mantle and local areas of melting or melt ponding.

A comparison of *P*- and *S*-wave relative arrival-time residuals for common station and event pairs is preferable to analysing directly the velocity anomalies on our tomographic images because problems associated with amplitude recovery (e.g. due to differing numbers of traveltime observations and regularisation levels) and other artefacts associated with the inversion procedure (such as parametrization and ray-path accuracy) do not complicate the comparison of the data. Fig. 9 shows the correlation between the *P* and *S* traveltime data. Gao *et al.* (2004) cite a slope of 2.9 on such a plot as characteristic of a purely thermal origin for the relative arrival-time residuals, based on the model of Karato (1993). Our data are consistent with a slope >2.9 further implying the presence of partial melt, especially beneath the rift (Fig. 9b).

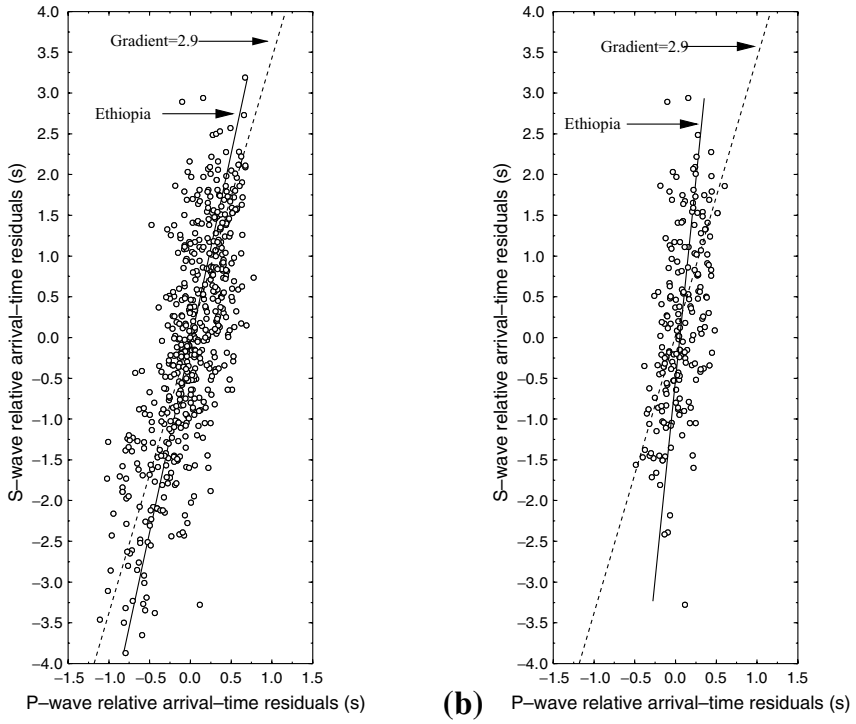

Figure 9. Plots of *P*-wave versus *S*-wave relative arrival-time residuals for common earthquakes and stations for (a) all stations, (b) stations within the rift valley. The dashed lines on the plot indicate a gradient of 2.9 for comparison with the results of Gao *et al.* (2004) and the solid lines are the least-squares fit to our data (gradients are ≈5 and ≈10 for plots (a) (all data) and (b) (rift valley data), respectively).

6.4 Implications for breakup and rifting models

These new tomographic images of upper-mantle structure illustrate complex interactions between pre-existing and strain (rifting) induced base-of-lithosphere topography and melt supply beneath a rift that is transitional between continental and oceanic rifting.

We have shown that our imaged low-velocity anomalies are likely the result of temperature affects and partial melt. We also know *a priori* that 80 per cent of the extension in the Ethiopian rift is now accommodated at Quaternary magmatic segments within the rift (Bilham *et al.* 1999). However, both traditional (e.g. Wernicke 1985) and more recent (e.g. Huismans & Beaumont 2003) kinematic models for rifting often ignore the effects of melt in the rifting process; and in doing so they ignore the observation that the average tectonic force required to initiate and maintain breakup may be up to an order of magnitude greater than that which is commonly available (e.g. Kusznir & Park 1987; Hopper & Buck 1993; Buck 2004). Buck (2004) quantifies the effect of diking in extensional systems, demonstrating the efficient reduction in mantle lithospheric thickness in the presence of melt. In this model, the combined effects of lithospheric heating by magma localizes thinning and facilitates extension at much smaller plate driving forces. Field observations of dike intrusions into the crust (e.g. Wolfenden *et al.* 2004), combined with seismic evidence for cooled mafic intrusions in the lower crust (Keranen *et al.* 2004) and our segmented along axis mantle low-velocity anomalies all point to a model of strain accommodation by magma injection.

The large border faults in the study area accommodated early extension (Hayward & Ebinger 1996). Our observed offset of upper-mantle low-velocity anomalies away from the magmatic segments in the centre of the rift towards the uplifted rift flanks indicates some linkage between the fault controlled strain and the development of the upper mantle along axis segmentation. This inference, however, is complicated by the presence of low-velocity structures beneath off-rift volcanic areas. Such observations show that pre-existing, as well as strain (rifting), induced base-of-lithosphere topography may play an important role in melt transport beneath the rift system.

Thus, our observations from this magmatic rift zone do not support detachment fault models of lithospheric extension, but instead point to strain accommodation by melt intrusion in progressively narrower zones (magmatic segments), which may mark the eventual breakup boundary (Buck 2004).

7 CONCLUSIONS

Relative arrival-time residuals show that the Ethiopian rift flanks are asymmetric in nature with faster arrivals associated with the Somalian Plate than the Ethiopian Plateau. This variation cannot be entirely explained by crustal thickness variations and implies either that the rift has formed at the joining of two distinct lithospheric units, or alternatively to the presence of low-velocity material beneath the western Ethiopian Plateau.

Independent tomographic inversion of *P*- and *S*-wave data show that the rift is underlain by low-velocity structures that are segmented in the uppermost 100 km of the mantle. The broadening and increasing depth extent of the low-velocity structures at depths >100 km towards Afar, is consistent with the longer history of rifting in the Red Sea and Aden rift systems, as well as with the Pliocene–Recent northward propagation of the Ethiopian rift as plate boundaries changed in the Afar triple junction zone.

Direct comparison of *P*- and *S*-wave relative arrival-time data indicates that high-temperature contrasts exist across the network. These high temperatures are likely to be accompanied by the presence of partial melt, especially beneath the rift.

The upper-mantle low-velocity anomalies are segmented along axis beneath the rift valley and are often displaced towards the flank of the rift where topography is greatest and the lithosphere–asthenosphere boundary is steepest.

Our observations from this magmatic rift zone, therefore, do not support detachment fault models of lithospheric extension but instead point to strain accommodation in progressively narrower zones (magmatic segments), which may mark the eventual breakup boundary. This work is consistent with the magma assisted rifting hypothesis of Buck (2004).

ACKNOWLEDGMENTS

We firstly thank John VanDecar for providing us with the inversion code used in this study and advice on its use. All members of the EAGLE working group (Maguire *et al.* 2003) provided fruitful discussions of the results. Drs Laike Asfaw and Atalay Ayele of the Geophysical Observatory, Addis Ababa University and their colleagues, Drs Bekele Abebe, Tilahun Mamo, Dereje Ayele and Gezahegn Yirgu of the Department of Geology and Geophysics are thanked for their support throughout this project. The Ethiopian Science Commission assisted with logistics. We thank the staff at SEIS-UK, particularly Alex Brisbourne, for their technical assistance in the data acquisition stage of the project. U. Achauer, A. Nyblade and G. Laske all provided helpful reviews, which improved the manuscript.

This project was supported by NERC grant NER/A/S/2000/01003 and a PhD NERC studentship NER/S/A/2001/06267.

REFERENCES

Abdelsalam, M. & Stern, R., 1996. Sutures and shear zones in the Arabian–Nubian Shield, *J. Afr. Earth Sci.,* **23**(3), 289–310.

Abebe, T., Mazzarini, F., Innocenti, F. & Manetti, P., 1998. The Yerer–Tullu Wellel volcanotectonic lineament: a transtensional structure in central Ethiopia and the associated magmatic activity, *J. Afr. Earth Sci.,* **26**(1), 135–150.

Achauer, U. & Masson, F., 2002. Seismic tomography of continental rifts revisited: from relative to absolute heterogeneities, *Tectonophysics,* **358,** 17–37.

Allen, R. *et al*., 2002. Imaging the mantle beneath Iceland using integrated seismological techniques, *J. geophys. Res.,* **107,** 2325.

Ayele, A., Stuart, G. & Kendall, J.-M., 2004. Insights into rifting from shear wave splitting and receiver functions; an example from Ethiopia, *Geophys. J. Int.,* **157,** 354–362.

Benoit, M., Nyblade, A., VanDecar, J. & Gurrola, H., 2003. Upper mantle P wave velocity structure and transition zone thickness beneath the Arabian Shield, *Geophys. Res. Lett.,* **30**(10), 1531, doi:10.1029/2002GL016436.

Berckhemer, H. *et al*., 1975. Deep seismic soundings in the Afar region and on the highland of Ethiopia, in *Afar Depression of Ethiopia,*Vol. I, pp. 89–107, eds Pilger, A. & Rösler, A., Schweizerbart, Stuttgart.

Bilham, R., Bendick, R., Larson, K., Mohr, P., Braun, J., Tesfaye, S. & Asfaw, L., 1999. Secular and tidal strain across the Main Ethiopian Rift, *Geophys. Res. Lett.,* **26,** 2789–2792.

Buck, W., 2004. Consequences of asthenospheric variability on continental rifting, in *Rheology and Deformation of the Lithosphere at Continental Margins,* pp. 1–30, eds Karner, G., Taylor, B., Driscoll, N.W. & Kohlstedt, D.L. Columbia University Press, NY, USA.

Chernet, T., Hart, W., Aronson, J. & Walter, R., 1998. New age constraints on the timing of volcanism and tectonism in the northern Main Ethiopian Rift—southern Afar transition zone (Ethiopia), *J. Volc. Geotherm. Res.,* **80,** 267–280.

Cline, A., 1981. *FITPAK—software package for curve and surface fitting employing splines under tension,* Department of Computer Sciences, University of Texas, Austin, TX.

Constable, S., Parker, R. & Constable, C., 1987. Occam's inversion: a practical algorithm for generating smooth models from electromagnetic sounding data, *Geophysics,* **52,** 289–300.

Courtillot, V., Jaupart, C., Manighetti, I., Tapponnier, P. & Besse, J., 1999. On causal links between flood basalts and continental breakup, *Earth planet. Sci. Lett.,* **166,** 177–195.

Davis, P. & Slack, P., 2002. The uppermost mantle beneath the Kenya dome and relation to melting, rifting and uplift in East Africa, *Geophys. Res. Lett.,* **29**(7), 10.1029/2001GL013676.

Debayle, E., Lévêque, J. & Cara, M., 2001. Seismic evidence for a deeply rooted low-velocity anomaly in the upper mantle beneath the northeastern Afro/Arabian continent, *Earth planet. Sci. Lett.,* **193,** 423–436.

Dugda, M., Nyblade, A., Julia, J., Langston, C., Ammon, C. & Simiyu, S., 2005. Crustal structure in Ethiopia and Kenya from receiver function analysis, *J. geophys. Res.,* **110**(B1), doi:10.1029/2004JB003065.

Ebinger, C. & Casey, M., 2001. Continental breakup in magmatic provinces: an Ethiopian example, *Geology,* **29,** 527–530.

Ebinger, C. & Sleep, N., 1998. Cenozoic magmatism throughout East Africa resulting from impact of a single plume, *Nature,* **395,** 788–791.

Ebinger, C., Bechtel, T., Forsyth, D. & Bowin, C., 1989. Effective elastic plate thickness beneath the East African and Afar plateaus and dynamic compensation of the uplifts, *J. geophys. Res.,* **94,** 2883–2901.

Evans, J. & Achauer, U., 1993. Teleseismic tomography using the ACH method: theory and application to continental scale studies, in *Seismic Tomography: Theory and Practice,* pp. 319–357, eds Iyer, H. & Hirahara, K., Chapman and Hall, New York.

Fernandes, R., Ambrousius, B., Noomen, R., Bastos, L., Combrinck, L., Miranda, J. & Spakman, W., 2004. Angular velocities of Nubia and Somalia from continuous GPS data: implications on present-day relative kinematics, *Earth planet. Sci. Lett.,* **222,** 197–208.

Gao, S., Liu, K., Davis, P. & Slack, P., 2003. Evidence for small scale mantle convection in the upper mantle beneath the Baikal rift zone, *J. geophys. Res.,* **108**(B4), 2194, doi:10.1029/2002JB002039.

Gao, W., Grand, S., Baldridge, W., Wilson, D., West, M., Ni, J. & Aster, R., 2004. Upper mantle convection beneath the central Rio Grande rift imaged by *P* and *S* wave tomography, *J. geophys. Res.,* **109**(B03305), doi:10.1029/2003JB002743.

Gashawbeza, E., Klemperer, S., Nyblade, A., Walker, K. & Keranen, K., 2004. Shear-wave splitting in Ethiopia: Precambrian mantle anisotropy locally modified by Neogene rifting, *Geophys. Res. Lett.,* **31,** doi:10.1029/2004GL020471.

George, R., Rogers, N. & Kelley, S., 1998. Earliest magmatism in Ethiopia: evidence for two mantle plumes in one continental flood basalt province, *Geology,* **26,** 923–926.

Goes, S., Govers, & Vacher, P., 2000. Shallow mantle temperatures under Europe from *P* and *S* wave tomography, *J. geophys. Res.,* **105**(B5), 11 153–11 169.

Gripp, A. & Gordon, R., 2002. Young tracks of hotspots and current plate velocities, *Geophys. J. Int.,* **150,** 321–361.

Hayward, N. & Ebinger, C., 1996. Variations in the along–axis segmentation of the Afar rift system, *Tectonics,* **15,** 244–257.

Hebert, L. & Langston, C., 1984. Crustal thickness estimate at AAE (Addis Ababa, Ethiopia) and NAI (Nairobi, Kenya using teleseismic *P*-wave conversions, *Tectonophysics,* **111,** 299–327.

van der Hilst, R., Engdahl, E. & Spakman, W., 1993. Tomographic inversion of *P* and *pP* data for aspherical mantle structure below the northwest Pacific region, *Geophys. J. Int.,* **115,** 264–302.

Hofmann, C., Courtillot, V., Feraud, G., Rochette, P., Yirgu, G., Ketefo, E. & Pik, R., 1997. Timing of the Ethiopian flood basalt event and implications for plume birth and global change, *Nature,* **389,** 838–841.

Holbrook, W. & Kelemen, P., 1993. Large igneous province on the US Atlantic margin and implications for magmatism during breakup, *Nature,* **364,** 433–436.

Hopper, J. & Buck, W., 1993. The initiation of rifting at constant tectonic force: the role of diffusion creep, *J. geophys. Res.,* **98,** 16 213–16 221.

Huismans, R. & Beaumont, C., 2003. Symmetric and asymmetric lithospheric extension: relative effects of frictional–plastic and viscous strain softening, *J. geophys. Res.,* **108**(B10), 2496, doi:10.1029/2002JB002026.

Karato, S., 1993. Importance of anelasticity in the interpretation of seismic tomography, *Geophys. Res. Lett.,* **20**(15), 1623–1626.

Kendall, J.-M., Stuart, G., Ebinger, C., Bastow, I. & Keir, D., 2005. Magma assisted rifting in Ethiopia, *Nature,* **433,** 146–148.

Kennett, B. & Engdahl, E., 1991. Traveltimes from global earthquake location and phase identification, *Geophys. J. Int.,* **105**(2), 429–465.

Keranen, K., Klemperer, S., Gloaguen, R. & EAGLE Working Group, 2004. Three-dimensional seismic imaging of a protoridge axis in the main Ethiopian rift, *Geology,* **32,** 949–952.

Knox, R., Nyblade, A. & Langston, C., 1998. Upper mantle S velocities beneath Afar and western Saudi Arabia from Rayleigh wave dispersion, *Geophys. Res. Lett.,* **25,** 4233–4236.

Kusznir, N. & Park, R., 1987. The extensional strength of the continental lithosphere: its dependence on geothermal gradient, and crustal composition and thickness, in *Continental Extensional Tectonics, Geological Society Special Publication,*Vol. 28, pp. 35–52, eds Coward, M.P., Dewey, J.F. & Hancock, P.L., Geological Society of London, London

Lister, G., Etheridge, M. & Symonds, P., 1986. Detachment faulting and the evolution of passive continental margins, *Geology,* **14,** 246–250.

Louden, K. & Chian, D., 1999. The deep structure of non-volcanic rifted continental margins, *Phil. Trans. R. Soc. Lond.,* **357,** 767–804.

Mackenzie, G., Thybo, H. & Maguire, P., 2005. Crustal velocity structure across the Main Ethiopian Rift: results from 2-dimensional wide-angle seismic modelling, *Geophys. J. Int.,* doi:10.1111/j.1365-246X.2005.02710.x.

Maguire, P. *et al*., 2003. Geophysics project in Ethiopia studies continental breakup, *EOS, Trans. Am. geophys. Un.,* **84**(35), 342–343.

Makris, J. & Ginzburg, A., 1987. The Afar Depression: transition between continental rifting and sea floor spreading, *Tectonophysics,* **141,** 199–214.

Menzies, M., Klemperer, S., Ebinger, C. & Baker, J., 2002. Characteristics of volcanic rifted margins, volcanic rifted margins, *Geol. Soc. Am. Spec. Pap.,* **362,** 1–14.

Mohr, P., 1967. Major volcanotectonic lineament in the Ethiopian rift system, *Nature,* **213,** 664–665.

Montelli, R., Nolet, G., Dahlen, F., Masters, G., Engdahl, E. & Hung, S.-H., 2004. Finite-frequency tomography reveals a variety of plumes in the mantle, *Science,* **303,** 338–343.

Nyblade, A., Knox, R. & Gurrola, H., 2000. Mantle transition zone thickness beneath Afar: implications for the origin of the Afar hotspot, *Geophys. J. Int.,* **142,** 615–619.

Peterson, J., 1993. *Observations and modelling of seismic background noise,* Open File Report, US Geological Survey, Denver, CO, pp. 93–322.

Poupinet, G., 1979. On the relation between P-wave travel time residuals and the age of the continental plates, *Earth planet. Sci. Lett.,* **43,** 149–161.

Ritsema, J. & Allen, R., 2003. The elusive mantle plume, *Earth planet. Sci. Lett.,* **207,** 1–12.

Ritsema, J., Nyblade, A., Owens, T., Langston, C. & VanDecar, J., 1998. Upper mantle seismic velocity structure beneath Tanzania, east Africa: implications for the stability of cratonic lithosphere, *J. geophys. Res.,* **103**(B9), 21 201–21 213.

Rooney, T., Furman, T., Yirgu, G. & Ayalew, D., 2005. Structure of the Ethiopian lithosphere: Evidence from mantle xenoliths, *Geochim. cosmochim. Acta,* in press.

Schimmel, M., Assumpção, M. & VanDecar, J., 2003. Seismic velocity anomalies beneath SE Brazil from P and S wave travel time inversions, *J. geophys. Res.,* **108**(B4), 2191, doi:10.1029/2001JB000187.

Sobolev, S., Zeyen, H., Stoll, G., Werling, F., Altherr, R. & Fuchs, K., 1996. Upper mantle temperatures from teleseismic tomography of French Massif Central including effects of composition, mineral reactions, anharmonicity and partial melt, *Earth planet. Sci. Lett.,* **139,** 147–163.

Sol, S., Thompson, C., Kendall, J.-M., White, D., VanDecar, J. & Asude, I., 2002. Seismic tomographic images of the cratonic upper mantle beneath the Western Superior Province of the Canadian Shield–a remnant Archaean slab, *Phys. Earth planet. Int.,* **134,** 53–69.

Tiberi, C., Diament, M., Déverchére, J., Petit-Mariani, C., Mikhailov, V., Tikhotsky, S. & Achauer, U., 2003. Deep structure of the Baikal rift zone revealed by joint inversion of gravity and seismology, *J. geophys. Res.,* **108**(B3), doi:10.1029/2002JB001880.

Tiberi, C., Ebinger, C., Ballu, V., Stuart, G. & Oluma, B., 2004. Inverse models of gravity data from the Red Sea—Aden—East African rifts triple junction zone, *Geophys. J. Int.,* submitted.

Tilmann, F., Benz, H., Priestly, K. & Okubo, P., 2001. P–wave velocity structure of the uppermost mantle beneath Hawaii from traveltime tomography, *Geophys. J. Int.,* **146,** 594–606.

Ukstins, I., Renne, P., Wolfenden, E., Baker, J., Ayalew, D. & Menzies, M., 2002. Matching conjugate volcanic rifted margins: $^{40}Ar/^{39}Ar$ chrono stratigraphy of pre– and syn–rift bimodal flood volcanism in Ethiopia and Yemen, *Earth planet. Sci. Lett.,* **198,** 289–306.

VanDecar, J., 1991. Upper-mantle structure of the Cascadia subduction zone from non-linear teleseismic travel time inversion, *PhD thesis*, University of Washington, Seattle.

VanDecar, J. & Crosson, R., 1990. Determination of teleseismic relative phase arrival times using multi-channel cross-correlation and least squares, *Bull. seism. Soc. Am.,* **80**(1), 150–169.

Vauchez, A., Barruol, G. & Tommasi, A., 1997. Why do continents break–up parallel to ancient orogenic belts?, *TerraNova,* **9,** 62–66.

Wernicke, B., 1985. Uniform–sense normal simple shear of the continental lithosphere, *Can. J. Earth Sci.,* **22,** 108–125.

WoldeGabriel, G., 1988. Volcanotectonic history of the central sector of the main Ethiopian rift; a geochronological, geochemical and petrological approach, *PhD thesis*, Case Western Reserve University, Cleveland, OH.

WoldeGabriel, G., Yemane, T., Suwa, G., White, T. & Asfaw, B., 1991. Age of volcanism and rifting in the Buri–Soyoma are, Amarco Horst, southern main Ethiopian Rift: geo- and biochronologic data, *J. Afr. Earth Sci.,* **13,** 437–447.

Wolfenden, E., Ebinger, C., Yirgu, G., Deino, A. & Ayalew, D., 2004. Evolution of the northern main Ethiopian rift: birth of a triple junction, *Earth planet. Sci. Lett.,* **224,** 213–228.